JACS
JOURNAL OF THE AMERICAN CHEMICAL SOCIETY
Article
pubs.acs.org/JACS

SSZ-13 Crystallization by Particle Attachment and Deterministic Pathways to Crystal Size Control

Manjesh Kumar,[†] Helen Luo,[‡] Yuriy Román-Leshkov,[‡] and Jeffrey D. Rimer*[,†]

[†]Chemical and Biomolecular Engineering, University of Houston, Houston, Texas 77204, United States
[‡]Chemical Engineering, Massachusetts Institute of Technology, Cambridge, Massachusetts 02139, United States

Supporting Information

ABSTRACT: Many synthetic and natural crystalline materials are either known or postulated to grow via nonclassical pathways involving the initial self-assembly of precursors that serve as putative growth units for crystallization. Elucidating the pathway(s) by which precursors attach to crystal surfaces and structurally rearrange (postattachment) to incorporate into the underlying crystalline lattice is an active and expanding area of research comprising many unanswered fundamental questions. Here, we examine the crystallization of SSZ-13, which is an aluminosilicate zeolite that possesses exceptional physicochemical properties for applications in separations and catalysis (e.g., methanol upgrading to chemicals and the environmental remediation of NO_x). We show that SSZ-13 grows by two concerted mechanisms: nonclassical growth involving the attachment of amorphous aluminosilicate particles to crystal surfaces and classical layer-by-layer growth via the incorporation of molecules to advancing steps on the crystal surface. A facile, commercially viable method of tailoring SSZ-13 crystal size and morphology is introduced wherein growth modifiers are used to mediate precursor aggregation and attachment to crystal surfaces. We demonstrate that small quantities of polymers can be used to tune crystal size over 3 orders of magnitude (0.1−20 μm), alter crystal shape, and introduce mesoporosity. Given the ubiquitous presence of amorphous precursors in a wide variety of microporous crystals, insight of the SSZ-13 growth mechanism may prove to be broadly applicable to other materials. Moreover, the ability to selectively tailor the physical properties of SSZ-13 crystals through molecular design offers new routes to optimize their performance in a wide range of commercial applications.

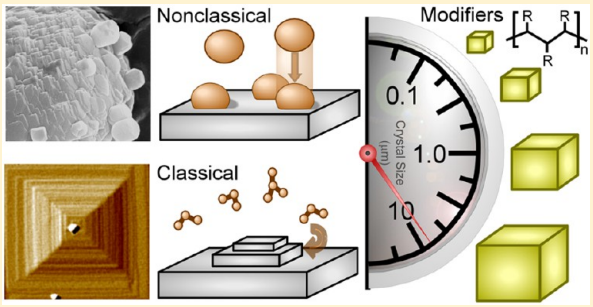

INTRODUCTION

Crystal engineering is a diverse area of research involving the design and optimization of materials for applications ranging from energy to medicine. Developing materials with predictable physicochemical properties is challenging due to the complex, and often unknown, mechanisms of crystal nucleation and growth. This is particularly true for materials that form via *nonclassical* pathways involving the attachment of precursors that range from multi-ion complexes and oligomers to primary particles and nanocrystallites. Crystallization by particle attachment (or CPA)[1] differs from classical mechanisms where two-dimensional layers on crystal surfaces are generated and advance via the addition of ions or molecules. Materials that grow by CPA pathways include diverse synthetic (e.g., noble metals, metal oxides, zeolites),[2−6] natural (e.g., iron oxides, magnetite, gypsum),[7−10] and biogenic (e.g., proteins, calcium carbonates/phosphates) crystals.[11−14] In many cases, crystallization involves multiple and invariably complex pathways.[15,16] For example, previous studies of zeolite silicalite-1 revealed that nucleation and growth occur by concerted events involving the addition/aggregation of amorphous silica nanoparticles (ca. 3 nm), the structural rearrangement of particles postattachment, and the addition of silica molecules.[16,17] Fundamental understanding of CPA mechanisms are reasonably limited, though much progress is being made as a result of advanced in situ electron and scanning probe microscopy imaging techniques,[14,18] which are capable of providing unprecedented insight into the dynamics and mechanisms of crystallization.

Zeolites are crystalline microporous materials that epitomize this expanding field of research due to their multifaceted growth solutions comprised of diverse species, which include (alumino)silicate molecules, oligomers, amorphous bulk phases, and nanoparticle precursors. The precursors that form in syntheses of zeolites and related materials (e.g., metal oxides)[19] often undergo a structural and/or compositional evolution during crystallization. The mere presence of precursors is suggestive of their potential role in crystal growth. Different zeolite growth mechanisms have been postulated in the literature, such as the direct attachment of primary particles, gel and/or solid-state transformations, and traditional layer-by-layer growth.[20] Gel transformation is the most commonly studied route wherein the initial condensation (or polymerization) of silica and alumina leads to the formation of heterogeneous sol gels with undefined microstructure. A common bulk precursor phase is irregular-shaped amorphous

Received: July 17, 2015
Published: September 16, 2015

DOI: 10.1021/jacs.5b07477
J. Am. Chem. Soc. 2015, 137, 13007−13017

wormlike particles (WLPs), which form during the induction period and are gradually consumed over the course of crystal growth.[21−24] There are two potential roles of WLPs in crystallization: as sites for heterogeneous nucleation or as sources of nutrient (i.e., soluble silica and alumina growth units). Obtaining time-resolved in situ data of zeolite growth is difficult owing to several factors: (i) slow kinetics of crystallization requires long sampling times, (ii) harsh synthesis conditions (e.g., high temperature, pressure, and pH) are difficult to reproduce with many imaging techniques, and (iii) nonideal physical properties of growth solutions (e.g., high viscosity, nonergodic, and opaque colloidal suspensions) render these systems inoperable to characterize by common analytical techniques, such as microscopy and scattering. This, in turn, leaves many questions pertaining to the pathway(s) of crystallization unanswered.

The zeolite SSZ-13 has garnered considerable attention based on its use in several commercial applications.[25−37] SSZ-13 is an important commercial catalyst in reactions such as amination (e.g., methylamines),[38] methanol to hydrocarbons (MTH),[37,39,40] and selective catalytic reduction (SCR) of NOx.[34,41−45] Copper-substituted SSZ-13 and its silicoaluminophosphate isostructural analogue SAPO-34 have unusually high thermal stability and low temperature activation in SCR reactions.[46] Moreover, Cu-SSZ-13 has the highest activity and N_2 formation selectivity in the oxidation of NH_3 relative to other microporous catalysts, for example, Cu-Beta and Cu-ZSM-5.[34,47,48] In MTH processes, SSZ-13 catalysts exhibit high selectivity for light olefins (C_2−C_4).[39]

The crystal structure of SSZ-13 (Figure 1) consists of two composite building units, double-six-membered rings (*d6r*) and

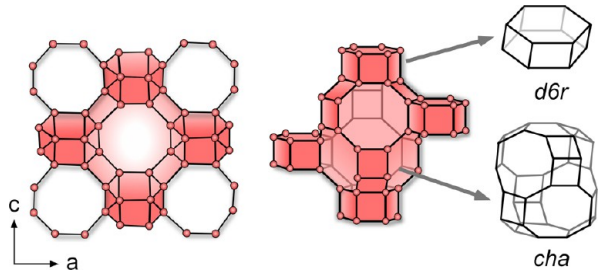

Figure 1. SSZ-13 (CHA framework type) is comprised of 8-membered ring pores. The crystal topology, shown here for the (010) face, is a trigonal structure (*R*3*m* space group). Interconnecting *d6r* and *cha* composite building units give rise to a three-dimensional network of pores.

cha cages, which are joined together to form a three-dimenional network of pores with 0.37 nm diameter windows connecting cages with a larger diameter of 0.74 nm. SSZ-13 was first synthesized by Zones and co-workers[49] using *N*,*N*,*N*-trimethyl-1-1-adamantammonium (TMAda) as an organic structure-directing agent (OSDA). Conventional SSZ-13 synthesis yields micron-sized crystals with cubic morphology; however, Zones also reported the synthesis of SSZ-62, which has an identical crystal structure with an average crystal size ≤500 nm.[50] Alternative methods to synthesize SSZ-13 have been reported, often focusing on ways to improve the economics by eliminating and/or reducing the quantity of OSDA, which is expensive and nonrecoverable.[35,36] Examples include intercrystalline conversion from a starting zeolite (e.g., FAU), the use of alternative OSDAs (e.g., benzyltrimethylammonium[51] and tetraethylenepentamine[36]), and the adjustment of synthesis parameters (e.g., Si/Al ratio)[52] to produce SSZ-13 crystals with dimensions ranging from 300 nm to about 5 μm.

Prior studies of SAPO-34 have shown that catalyst lifetime in MTH reactions can be substantially increased with decreased particle size,[53] whereas other groups[54,55] have shown that the introduction of mesoporosity in SSZ-13 crystals improves their catalytic performance. Similar structure-performance relationships have been reported for ZSM-5 catalysts in MTH reactions; however, it has been demonstrated that smaller crystal size is not always better—notably, larger ZSM-5 catalysts (ca. 20 μm) provide the best selectivity for light olefins in MTH reactions.[56] Collectively, these findings point to the inherent advantage of designing *tunable* syntheses that allow for the preparation of crystals with a broad and predictable range of sizes (a level of control that we seek to establish for SSZ-13 synthesis).

Herein, we present an ex situ time-resolved investigation of SSZ-13 crystallization using a synergistic combination of electron microscopy, atomic force microscopy, and X-ray/light scattering to elucidate the putative pathways of crystal growth. We track the formation and structural evolution of amorphous precursors and provide evidence that growth occurs via the direct attachment of precursors to crystal surfaces, followed by their structural rearrangement (postattachment) to integrate into the underlying crystalline interface. Crystallization by particle attachment seemingly plays a dominant role, leading to the formation of spheroidal, highly roughened crystals; however, evidence of coarsening and the emergence of layered surfaces with prolonged heating time are indicative of growth by molecule addition, thus signifying a dual mechanism of crystallization involving both classical and nonclassical pathways. Based on these findings, we demonstrate that SSZ-13 crystallization can be selectively tailored through the use of crystal growth modifiers, which are molecules or macromolecules (e.g., polymers) with a propensity for interacting with crystal surfaces and either inhibiting or promoting their rate of growth. The judicious selection of modifiers or binary combinations thereof leads to crystal sizes spanning 100 nm to 20 μm, and a morphology that can be deterministically switched between a sphere and a cube.

EXPERIMENTAL SECTION

Materials. The following chemicals were purchased from Sigma-Aldrich (St. Louis, MO): poly(diallyldimethylammonium chloride) (PDDAC, MW = 150k, 20% in water), 1,2-hexanediol ($D6_{1,2}$, 98%), polyethylenimine (PEIM, 50 wt % in water, MW = 1300), 1,2,3-hexanetriol (BIOXTRA, ≥98.0%), 1,3-butanediol (99%), triethylenetetramine (≥97%), poly(vinyl alcohol) (80% hydrolyzed, MW = 9k−10k), and hexadecyltrimethylammonium bromide (CTAB, BioXtra, ≥99%). Additional reagents used for the synthesis of SSZ-13 include Cab-O-Sil (M-5, Spectrum Chemical), sodium hydroxide (98% pellets, MACRON Fine Chemicals), *N*,*N*,*N*-trimethyl-1-1-adamantammonium hydroxide (25 wt % in water, SACHEM Inc.), and aluminum hydroxide (80.3 wt % $Al(OH)_3$, SPI0250 hydrogel). Deionized (DI) water used in all experiments was purified with an Aqua Solutions RODI-C-12A purification system (18.2 MΩ). All reagents were used as received without further purification.

Preparation of SSZ-13 Crystals. SSZ-13 crystals were synthesized with the organic structure-directing agent *N*,*N*,*N*-trimethyl-1-1-adamantammonium hydroxide (TMAda-OH) using solutions with molar composition 0.052 $Al(OH)_3$:1.0 SiO_2:0.2 NaOH:44 H_2O:0.1 TMAda-OH. Sodium hydroxide (0.09 g, 0.0022 mol) was first dissolved in water (8.21 g, 0.4959 mol), followed by the addition of TMAda-OH (0.95 g, 0.0011 mol). This solution was stirred until clear

DOI: 10.1021/jacs.5b07477
J. Am. Chem. Soc. 2015, 137, 13007−13017

(ca. 15 min). Aluminum hydroxide (0.05 g, 0.0005 mol) was added to the solution and left to stir for another 15 min at room temperature. To this clear solution was added the silica source (0.67 g, 0.0112 mol), and the resulting mixture was stirred for 4 h. Crystals synthesized by this procedure are referred to as the *control*. For studies of SSZ-13 synthesis in the presence of organic growth modifiers, the additive of choice was added to the growth solution in a specific molar ratio xZGM/SiO_2 (or weight percentage of the entire growth solution) after OSDA addition, but prior to the addition of the alumina source. Approximately 10 g of growth solution was placed in a Teflon-lined stainless steel acid digestion bomb (Parr Instruments) and was heated under rotation (~30 rpm) and autogenous pressure in a Thermo-Fisher Precision Premium 3050 Series gravity oven. The nominal time and temperature for SSZ-13 synthesis was 6 days at 180 °C. The products of all syntheses were isolated as a white powder (ca. 600 mg) by centrifuging the mother liquor (13 000 rpm for 45 min) for three cycles with DI water washes. Samples for microscopy were prepared by first redispersing a small amount of powder (ca. 5 mg) in DI water. An aliquot of this solution was placed on a glass slide and dried overnight. Crystals were transferred to metal sample disks for microscopy studies by contacting the glass slide with either carbon tape for SEM or partially cured epoxy for AFM (for details, please refer to our previous publication[16]).

Materials Characterization. Powder X-ray diffraction (XRD) patterns of as synthesized samples were collected on a Siemens D5000 X-ray diffractometer using a Cu Kα source (40 kV, 30 mA). The XRD patterns were indexed with a reference for SSZ-13 obtained from the International Zeolite Association structure database (Figure S1 in the Supporting Information, SI). Atomic force microscopy (AFM) was performed with a MFP-3D-SA instrument (Asylum Research, Santa Barbara, CA). Samples were prepared by transferring crystals from the glass slide to an AFM specimen disc (Ted Pella) coated with a thin layer of partially cured Loctite Epoxy Quickset (Henkel Corporation), which was then fully cured in an oven to firmly secure the crystals on the sample disc. Images were obtained in tapping mode with an Olympus RC800PB probe (0.8 N/m) at 256 scans/line and a 1.2 hz scan rate. Scanning electron microscopy (SEM) images were obtained with a FEI 235 dual-beam (focused ion-beam) system operated at 15 kV and a 5 mm working distance. All SEM samples were coated with a thin carbon layer (ca. 20 nm) prior to imaging. Textural analysis of the crystals was performed with a Micromeritics ASAP 2020 instrument using Ar as a probe gas for physisorption with an incremental dosing rate of 3 m^3/g STP and an analysis bath temperature of 77 K. Prior to analysis, samples were calcined at 550 °C for 4 h under flow of compressed air at 200 cm^3/min. The surface area was calculated from BET analysis selecting initial low pressure points with a correlation coefficient greater than 0.999. The weight percentage of occluded organics in SSZ-13 samples was assessed by thermogravimetric analysis (TGA) using a TA Instruments Q50 model and nitrogen as the carrier gas at a flow rate of 60 mL/min. The temperature was ramped up to 700 °C at the rate of 2 °C/min with an isothermal dwell time of 10 min. Elemental analysis was performed with inductively coupled plasma optical emission spectroscopy (ICP-OES) at the ICP Analytical Laboratory and Agilent Facility Center (University of Houston). Transmission electron microscopy images under cryogenic conditions (cryo-TEM) and selected area electron diffraction (SAED) patterns were acquired on a JEOL 2011 instrument equipped with a CCD camera at an operating voltage of 200 kV. The specimen was prepared by suspending the dried sample in acetone, and depositing a small droplet of the suspension on a TEM grid with a porous carbon film (Electron Microscopy Sciences). The sample grid was mounted on a Gatan cold stage and imaged at 100−103 K. ^{27}Al solid-state magic angle spinning nuclear magnetic resonance (MAS NMR) spectra were recorded using a Bruker DSX 500 spectrometer operating at 11.7 T with 130.3 MHz for ^{27}Al, using a Bruker 4 mm CPMAS probe. Spinning rates of 15 kHz were used and MAS spectra were recorded after applying a 0.3 μs-π/18 pulse with a recycle delay of 2 s and around 500 scans.

RESULTS AND DISCUSSION

Preparation of Control Samples. SSZ-13 crystals prepared by the nominal growth condition (referred to as the control) have a spheroidal morphology with an average dimension of 2.4 ± 0.3 μm (Figure 2A). The shape of control

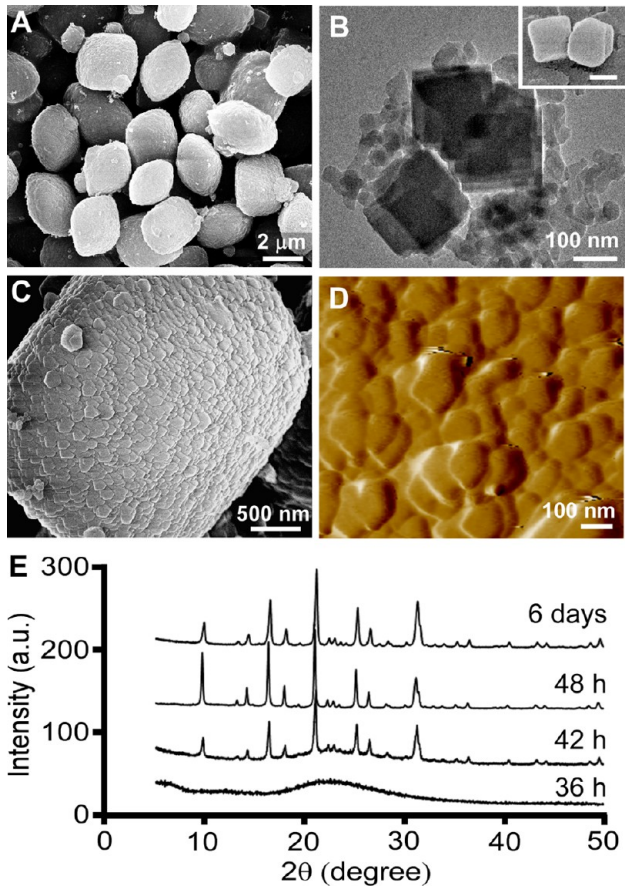

Figure 2. Characterization of SSZ-13 control crystals: (A) SEM image showing a population of crystals with average size 2.4 μm (based on measurements of more than 50 crystals from 3 separate batches); (B) TEM image of a sample after 42 h of heating showing a nascent population of small cubic crystals (inset: SEM image of cubic crystals after 6 days of heating; scale bar = 100 nm); and (C) high magnification SEM image of a single SSZ-13 crystal reveals a rough surface topography. (D) AFM amplitude mode image of a crystal surface in air shows the presence of layers with macrosteps (>10 nm height; see Figure S2). (E) Powder XRD patterns of samples extracted from a growth solution at periodic times: 36 h, 42 h, 48 h, and 6 days.

crystals deviates from the cubic morphology commonly reported in the literature for SSZ-13 and SAPO-34.[57] Powder XRD patterns (Figure S1) confirmed the formation of fully crystalline SSZ-13 (CHA framework type) after 6 days of heating without any impurities or residual amorphous material. Interestingly, the control sample contains a population of small crystals (ca. 200 nm) with cubic geometry. TEM images of samples extracted from growth solutions at early synthesis times (42 h, Figure 2B) show the initial formation of cubic crystals. The average size of these crystals remains relatively constant over a 6 day period of heating (Figure 2B, inset). The quantity of small crystals varies from batch to batch, but always accounts for a minor percentage of the total crystal population. In SEM images, small crystallites are observed on the surface of

DOI: 10.1021/jacs.5b07477
J. Am. Chem. Soc. 2015, 137, 13007−13017

larger particles, which may be attributed to adhesion during sample drying or possible aggregation in situ. High resolution electron micrographs of control crystals (Figure 2C) reveal roughened surfaces comprised of three-dimensional features (e.g., layers or protrusions) with similar dimensions equal to 186 ± 56 nm. AFM topographical images of SSZ-13 crystal surfaces confirmed the presence of layers (Figure 2D) with step heights that exceed 10 nm.

We studied the temporal evolution of particulates by characterizing the solids extracted from growth solutions after various heating times to track the amorphous-to-crystalline phase transition. The evolution of particle morphology and crystallinity was monitored by ex situ SEM and XRD, respectively. Time-resolved analysis of SSZ-13 growth encompassed the induction period (i.e., prenucleation) and intermediate times when the sample contained a partially crystalline product. Powder XRD patterns of extracted solids (Figure 2E) indicate that the induction period lasts approximately 30−40 h. The time frame for crystal growth is substantially faster than nucleation (i.e., full crystallinity is attained in less than 10 h). The induction period for the control is uncharacteristically long for a synthesis that occurs at high temperature (i.e., 180 °C) and high silica/alumina supersaturation. The 4-fold difference between nucleation and crystallization time suggests the early stage(s) of SSZ-13 synthesis involves slow processes encumbered by potentially high activation barriers. The long induction period is even more surprising considering the synthesis of SSZ-13 involves rotation, which reduces diffusion limitations. Moreover, the presence of an OSDA is expected to facilitate faster growth of the CHA framework by directing the assembly of *d6R* and *cha* building units (see Figure 1).

SEM images of samples within the first 12 h of heating reveal that amorphous precursors exhibit a spheroidal morphology with average diameter 76 ± 10 nm (Figure S3A and B). At longer heating time, the spheroidal particles appear to aggregate and fuse together, forming branched clusters (Figure 3B) that resemble the *wormlike particles* (WLPs) observed as precursors in growth solutions of other zeolites, such as MFI, TON, LTL, and GIS framework types.[21,22] After 24 h of heating, there is a slight increase in WLP width (81 ± 12 nm, Figure S3C and D); however, we observe an eventual plateau in WLP size toward the end of the induction period. Representative electron micrographs of fully grown WLPs in Figure 3A and B reveal an average WLP width of 90 ± 5 nm. Samples extracted from growth solutions between 30 and 42 h of heating exhibit two distinct populations of particles: spheroidal SSZ-13 crystals (2.8 ± 0.6 μm) and amorphous WLPs (Figure S4). This observation is consistent with the XRD pattern of a 42 h sample in Figure 2E indicating a partially crystalline product. The surfaces of SSZ-13 crystals in electron micrographs (Figures 3C and S4) exhibit distinct domain sizes and shapes that are commensurate with those of WLPs. TEM images (Figure 3D) and selected area electron diffraction (SAED) patterns in Figure 3E and F confirmed the presence of two different populations: amorphous WLPs (region i) and SSZ-13 crystals (region ii). After 48 h, the XRD pattern indicates that the product is fully crystalline, which is consistent with SEM images showing that WLPs are completely consumed. However, we still observe two distinct crystal populations where WLPs are seemingly replaced with nanocrystals having an average size of 133 ± 21 nm and cubic habit (Figure S5). We monitored changes in particle size and population density over longer times (ca. 72 h) and

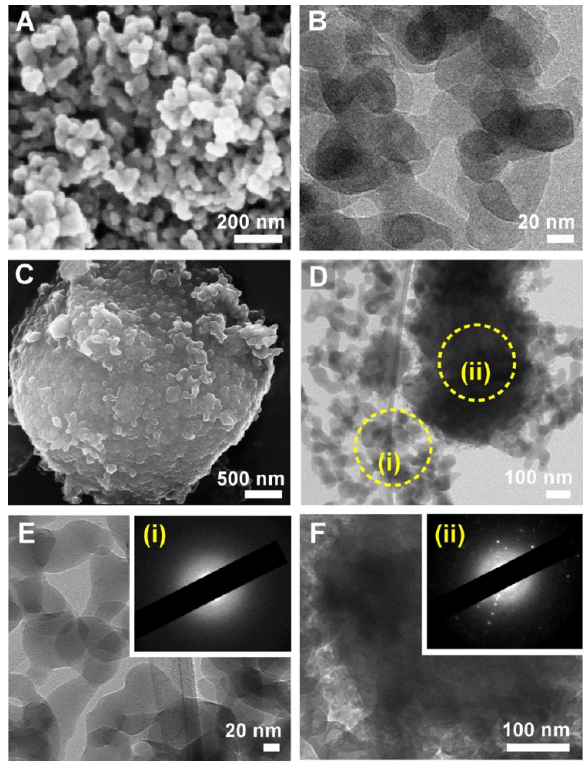

Figure 3. Control samples heated for (A, B) 36 h and (C−F) 42 h at 180 °C. The 36 h sample is predominantly comprised of WLPs, which was verified by (A) SEM and (B) cryo-TEM. SAED patterns of WLPs revealed no signs of crystallinity (see Figure S6 in the SI). (C) SEM image of a sample heated for 42 h reveals that spheroidal crystal surfaces are highly corrugated. (D) Cryo-TEM image showing the presence of two populations: (i) spheroidal crystals and (ii) WLPs. SAED patterns of regions i and ii in panel (D) reveal that (E) WLPs are amorphous and (F) spheroidal particles are crystalline, respectively.

observed that the size of nanocrystals increases to 292 ± 30 nm. After heating the growth solution for 6 days, the nanocrystals predominantly disappear, possibly due to ripening, in favor of a single population of SSZ-13 crystals with spheroidal morphology (Figure 2A).

The elemental composition of the solids and supernatant solution were tracked over a 42 h period of heating spanning several stages of growth, including the induction period (i.e., amorphous precursors), intermediate times during SSZ-13 formation (i.e., partially crystalline samples), and the final product (i.e., crystalline SSZ-13). Interestingly, the Si and Al content of the solids remains relatively constant during the induction period and throughout crystallization without any apparent discontinuity or changes around the time of nucleation. The Si/Al ratios of solids obtained from electron dispersive X-ray spectroscopy are consistent with the values measured by inductively coupled plasma optical emission spectroscopy (Figure S7). ICP-OES measurements of the supernatant solution after centrifugation and filtration (0.2 μm membrane) to remove large particulates revealed a monotonic increase in the Si/Al ratio that nearly doubles over the course of crystallization. The supernatant solution is silica-rich (Si/Al > 1000) and its Si/Al ratio has larger error compared to the solids, which suggests there is a higher degree of fluctuation in solution composition (see Figure S7).

DOI: 10.1021/jacs.5b07477
J. Am. Chem. Soc. 2015, 137, 13007−13017

Putative Pathways of Crystallization. SSZ-13 growth solutions are composed of silica, alumina, and/or aluminosilicate molecules (soluble species) and amorphous bulk phase precursors observed in electron micrographs. These precursors are present throughout crystallization and only decrease in number, but not in size. This seems to suggest that precursors are consumed by their direct attachment to SSZ-13 crystal surfaces, in stark contrast to a pathway involving precursor dissolution and temporal reduction in their size to generate soluble species that are concomitantly consumed by the growing crystals. These two scenarios are illustrated in Scheme 1. Crystal growth by the direct addition of molecules occurs via

Scheme 1. Illustration of Potential Classical (I) and Nonclassical (II) Pathways of SSZ-13 Crystallization[a]

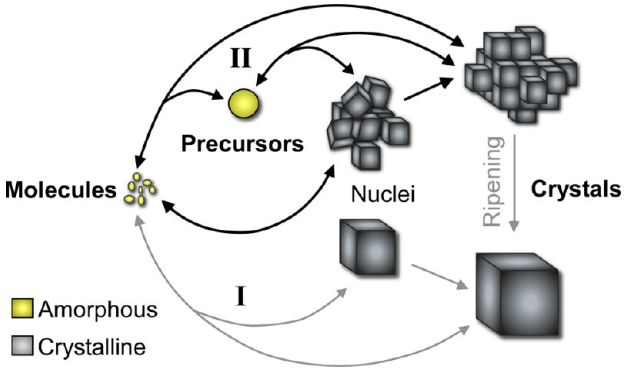

[a]Amorphous precursors and molecules (soluble species) labelled in yellow are possible growth units.

a layer-by-layer mechanism that typically leads to well-defined crystal habit (classical pathway I in Scheme 1).[58,59] Particle-mediated growth via the attachment and subsequent rearrangement of amorphous precursors is more likely to result in the formation of crystals with irregular morphology and/or rough surface features (nonclassical pathway II in Scheme 1).[16,60,61] Inferences from SEM and TEM images collectively suggest that precursor addition is the most likely mechanism of SSZ-13 growth. Notably, there are several indicators of nonclassical pathways gleaned from ex situ data: (i) crystals are spheroidal and lack distinct facets; (ii) crystal surfaces are composed of protrusions with domain sizes that are equivalent to those of precursors; and (iii) AFM topographical images of crystal surfaces (Figures 2D and S2) reveal the presence of 3D islands with large step heights (10−20 nm).

Figure 4 shows the spheroidal morphology and macroscopically rough surfaces of SSZ-13 crystals. Figure 4A and B shows representative images of crystals extracted from growth solutions prior to the completion of crystallization. The powder XRD pattern of this sample (Figure 2E) reveals the presence of residual amorphous material. High resolution SEM images of the crystal surface (Figure 4B) differentiate unique features labeled i−iii that refer to (i) large protrusions (0.5−1 μm) hypothesized to be aggregates of precursors, (ii) spheroidal particles attached to the surface that are potentially the remnants of WLPs that have undergone partial dissolution and/or structural rearrangement, and (iii) smaller islands (<100 nm) on the crystal surface. It is difficult to rationalize such features arising from processes governed solely by molecule addition. Indeed, classical layer-by-layer growth involves the generation and advancement of layers with step heights that are

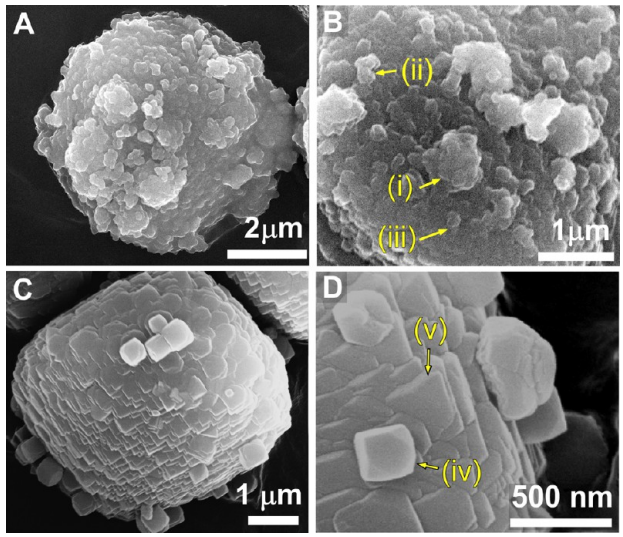

Figure 4. Scanning electron micrographs of SSZ-13 crystals at various synthesis times suggest a nonclassical pathway of growth via the direct addition of amorphous precursors. Here we compare samples heated for two different times: 42 h (A, B) and 48 h (C, D). Specific surface features i−v are labeled on high magnification SEM images in panels (B) and (D).

commensurate with the unit cell dimensions of the crystal (i.e., single layers or step bunches with heights on the order of 1 nm). SEM images of fully crystalline samples (Figure 4C and D) reveal the presence of macrosteps on crystal surfaces that are likely attributed to 3D layer generation, consistent with the proposed mechanism of particle-mediated growth. Surface features seemingly undergo a spheroidal-to-cubic (or rounded-to-faceted) transformation in morphology (e.g., feature *iv* in Figure 4D) with increased heating time. We also observe the presence of distinct terraces (e.g., feature *v* in Figure 4D) that coarsen over time, rendering crystal surfaces in SEM images visibly less rough.

A pathway wherein WLPs function as SSZ-13 growth units must also involve a disorder-to-order transition taking place postattachment to facilitate the incorporation of amorphous precursors into the underlying crystalline interface. Similar mechanisms have been shown to occur during the growth of calcium phosphate crystals[12,13] and also in the formation of silicalite-1 (MFI framework type) where the addition of amorphous (or disordered) precursors is accompanied by postattachment structural rearrangement.[16] Molecular-level details of these structural transformations are not well understood and may involve a combination of solid state rearrangement or solution-mediated processes (for example, ripening wherein precursors dissolve to produce molecules that reprecipitate on crystal surfaces). Notably, cryo-TEM images of SSZ-13 crystals extracted from synthesis solutions during growth (Figure 5A) reveal an external layer of small particulates with sizes less than 10 nm surrounding the crystals. Nearly every crystal observed in electron micrographs possesses an exterior *shell* of small particles. In contrast, regions on cryo-TEM samples populated with only WLPs, including samples extracted from growth solutions during the induction period, do not contain these smaller particles. In high resolution TEM (HRTEM) images we observe what appears to be precursor attachment to the surface (feature i in Figure 5B), and groupings of smaller particles (feature ii in Figure 5B).

DOI: 10.1021/jacs.5b07477
J. Am. Chem. Soc. 2015, 137, 13007−13017

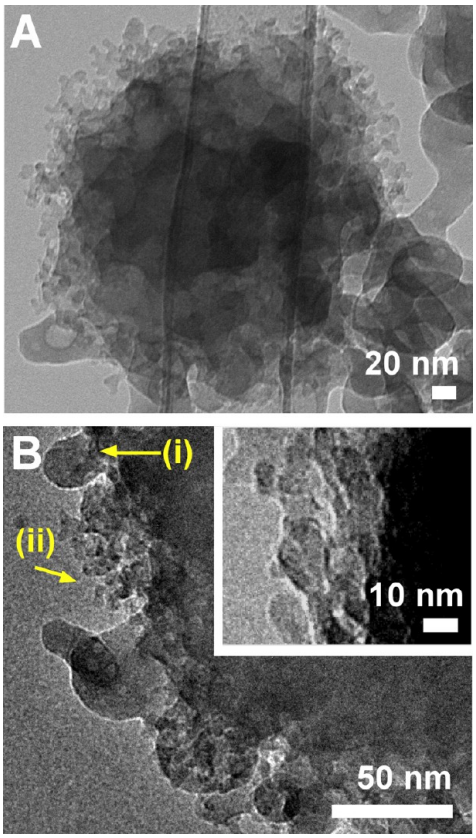

Figure 5. Cryo-TEM images of a control sample heated for 42 h. (A) Spheroidal crystals in all images appear to be surrounded by a layer of small particulates. (B) A high magnification image reveals the presence of spheroidal protrusions with sizes that are comparable to WLPs (feature i). There are also smaller particulates (feature ii) in close vicinity to the crystal surface that are not observed in regions heavily populated with WLPs or in samples extracted during the induction period (i.e., prenucleation samples containing only WLPs). Inset: magnified view of a crystal surface shows that these features exhibit a distribution of sizes that are predominantly less than 10 nm.

We checked for the presence of smaller particles in growth solutions by first removing the majority of WLPs and crystals by centrifugation and filtration (0.2 μm membrane), then analyzing the supernatant by dynamic light scattering (DLS) and small-angle X-ray scattering (SAXS). DLS measurements of solutions that were heated for 12−42 h revealed the presence of WLPs (Figure S8). CONTIN analysis[62] of DLS autocorrelation functions confirmed a single population of particles with sizes larger than 100 nm. Likewise, SAXS patterns (Figure S9) contain no evidence of particles smaller than 10 nm. The absence of small particles in DLS and SAXS analyses of growth solutions, coupled with cryo-TEM images showing their close proximity to crystal surfaces (and absence near amorphous bulk phases), suggests that the small particles are intermediate species generated near the crystal interface during the structural rearrangement of precursors. To our knowledge, few studies of CPA capture intermediate stages of precursor rearrangement; however, details of this process at the molecular level remain elusive.

To briefly summarize, we have provided evidence that SSZ-13 crystallization occurs via particle attachment, as illustrated in Scheme 1. In the following sections we present a facile and highly versatile method to control precursor aggregation and attachment to SSZ-13 surfaces in order to selectively modify crystal size and morphology.

Tailoring SSZ-13 Crystal Size. Using knowledge of the SSZ-13 growth mechanism, we mediate the kinetics of crystallization with concomitant effects on bulk crystal properties using *zeolite growth modifiers* (ZGMs), which are molecules or macromolecules that physisorb on specific crystallographic faces and alter the rate(s) of anisotropic growth.[63−67] We previously showed that the size and morphology of MFI and LTL crystals can be effectively altered with ZGMs.[68,69] One defining feature of modifier−crystal interactions is the molecular recognition that drives their preferential binding to a particular crystal surface. Conversely, adsorbates that lack such specificity are capable of binding to all crystal faces and alter growth rates isotropically and/or inhibit aggregation. Alternative nomenclatures in the literature for molecules that achieve similar ends include *particle-capping agents* (PCAs)[70,71] and *colloidal stabilizers*.[72,73] There are many examples of colloidal stabilizers used to control the growth of crystals, such as metals and metal oxides.[74−77] Common stabilizers include polymers, which are effective in their ability to introduce steric hindrance (the so-called "bumper effect" in colloidal dispersions);[78] however, depending on the concentration and/or molecular functionality of the polymer, the possibility exists for adsorbed polymers to bridge multiple surfaces and facilitate intercrystalline aggregation (the so-called "sticker effect" in colloidal dispersions).

We screened putative modifiers of SSZ-13 crystallization using organic molecules and polymers with different functional moieties. The most effective modifiers are listed in Table 1,

Table 1. Molecular Structure of the OSDA and ZGMs

Chemical	Molecular structure
Structure-directing agent	
N,N,N-trimethyl-1-1 -adamantammonium (TMAda)	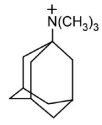
Modifier	
Polyethylenimine (PEIM) (M_n = 1.2k)	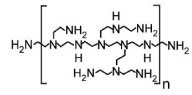
Cetyltrimethylammonium bromide (CTAB)	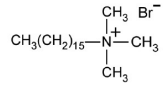
1,2-hexanediol ($D6_{1,2}$)	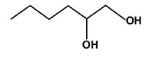
poly(diallyldimethylammonium chloride) (PDDAC) (M_w = 100k - 200k)	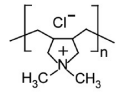

whereas less effective candidates are listed in Figure S10 of the SI. Among the modifiers tested, polyethylenimine (PEIM) has a notable impact on SSZ-13 crystal growth. Introduction of 1.0 wt % PEIM in the SSZ-13 growth solution resulted in ca. 1.0 μm crystals (Figure 6A) and generated macroscopically smoother and more monodisperse crystals relative to those prepared in the absence of modifier (i.e., control). Higher

DOI: 10.1021/jacs.5b07477
J. Am. Chem. Soc. 2015, 137, 13007−13017

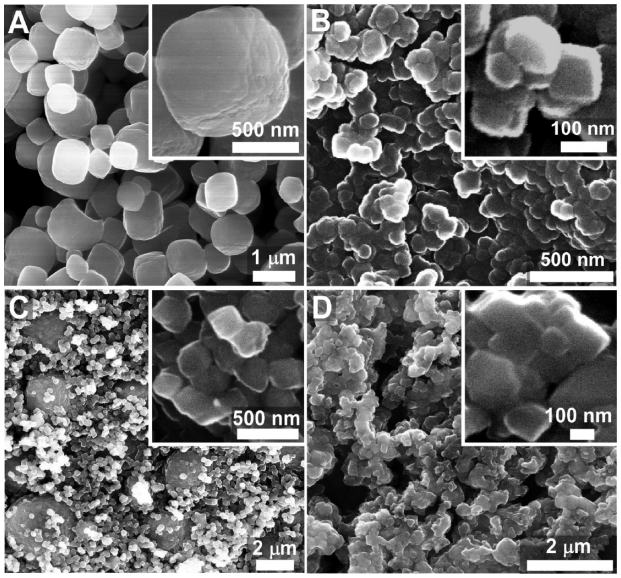

Figure 6. Scanning electron micrographs of SSZ-13 crystals prepared in the presence of growth inhibitors. (A, B) SEM images of crystals prepared at two different concentrations of PEIM: (A) 1 wt % and (B) 1.6 wt %. (C) SSZ-13 crystals prepared in the presence of 13.5 wt % 1,2-hexanediol ($D6_{1,2}$) exhibit a bimodal distribution of small and large crystallites. (D) Image of SSZ-13 crystals that were prepared with 7.5 wt % CTAB and calcined to remove the surfactant (see powder XRD patterns in Figure S14). Insets in all panels are high magnification images of representative crystals.

PEIM concentration (1.6 wt %) resulted in a 10-fold reduction in crystal size to 133 ± 30 nm (Figure 6B), which is the smallest size reported for SSZ-13. Although the exact mechanism for its mode of action is unknown, it is likely that PEIM functions as a colloidal stabilizer by adsorbing on crystal and/or precursor surfaces and inhibiting growth by particle attachment via steric stabilization. Scanning electron micrographs (Figure 6B) revealed that the majority of PEIM-modified nanocrystals are grouped into small clusters, which are either polycrystalline particles or aggregates that potentially form during SEM sample preparation.

SSZ-13 precursors and crystals exhibit negative surface charge due to the presence of dissociated silanol groups and tetrahedrally coordinated framework aluminum. The functional moieties of PEIM are composed of secondary and primary amines (Table 1). Dissociation constants for the amine groups in branched PEIM polymers are reported in the literature as pK_a < 10 (with variations depending on the polymer's molecular weight).[79] The pK_a of the modifier is well below the pH of the SSZ-13 growth solution (ca. pH 13). Under these conditions, PEIM is charge neutral and exhibits weak van der Waals or hydrophobic interactions with SSZ-13 precursors and crystals. PEIM-containing growth solutions lead to a substantial increase in the number of crystals, which suggests the modifier influences SSZ-13 nucleation.

Moreover, WLPs formed in the presence of PEIM are much smaller than those in control growth solutions; that is, the average width of PEIM-modified WLPs is 60 nm (Figure S11) compared to the nominal size of 100 nm. These observations collectively suggest that PEIM suppresses precursor aggregation and inhibits the kinetic rate of crystal growth; however, there is a practical upper limit in PEIM concentration for the preparation of SSZ-13 growth solutions. For instance, attempts to further decrease the size of SSZ-13 crystals by using a higher concentration of PEIM (e.g., 3.2 wt %) resulted in the formation of crystal polymorphs (XRD patterns of these samples are provided in Figure S12).

We characterized the physicochemical properties of SSZ-13 crystals prepared with PEIM relative to the control sample (Table 2). Elemental analysis (ICP-OES) revealed that PEIM has very little impact on the silicon-to-aluminum ratio, resulting in a change in Si/Al from 14.9 to 15.6. Moreover, solid state ^{27}Al NMR revealed that there is only a minor increase in the extra-framework aluminum content relative to the control SSZ-13 sample (Table 2 and Figure S13). These results are desirable outcomes from the standpoint of crystal engineering, i.e. the ability to tailor crystal size without significantly altering its chemical composition. Argon adsorption/desorption revealed that crystals prepared with PEIM have marginally higher specific surface area (532 m^2/g) relative to that of the control sample (504 m^2/g). Additionally, we quantified the residual mass of PEIM in SSZ-13 samples that were recovered from growth solutions after centrifugation and washing with DI water. Thermogravimetric analysis (TGA) of the control sample revealed a 13.2% weight loss attributed to the OSDA occluded within zeolite pores. The temperature-programmed TGA profile of the PEIM sample is nearly identical to that of the control (Figure S15); and the total weight loss of organic in the former is 14.3%, which indicates that SSZ-13 crystals retain only a small fraction of PEIM. The fact that a majority of polymer is removed during postsynthesis rinsing has practical implications for the recovery and recycling of modifiers in commercial SSZ-13 synthesis (i.e., reduced manufacturing costs).

Table 2. Physicochemical Properties of SSZ-13 Crystals

sample	size (μm)	S_A (m^2/g)[a]	Si/Al[b]	$Al_{(EF)}$ (%)[c]	TGA (wt % loss)[d]
control	2.4	504	14.9	1.7	13.2
PEIM[e]	0.1	532	15.6	2.4	14.3
PDDAC[e]	23.0	695	16.8	5.3	13.5

[a]BET surface area (*t*-plot analysis is provided in Table S1). [b]Measured by ICP−OES. [c]Extra-framework Al (mol %) measured by ^{27}Al NMR (Figure S13). [d]Weight loss of organic, excluding water (Figure S15). [e]Growth solutions prepared with 1.6 wt % PEIM and 0.5 wt % PDDAC.

There were two additional modifiers tested in this study that also reduced the size of SSZ-13 crystals: 1,2-hexanediol ($D6_{1,2}$), which was one of the most effective modifiers identified in prior studies of LTL;[69] and the surfactant cetyltrimethylammonium bromide (CTAB), which was selected on the basis of its potential to act as a colloidal stabilizer to minimize precursor aggregation. As shown in Figure 6C, the presence of $D6_{1,2}$ in SSZ-13 growth solutions leads to 290 nm crystals, which is slightly larger than PEIM-modified crystals. One distinguishing feature of $D6_{1,2}$ is its inability to fully suppress the formation of larger (ca. 2 μm) SSZ-13 crystals. The lower efficacy of $D6_{1,2}$ compared to PEIM may be attributed to its small size relative to the polymer. Indeed, a prior study of zeolite L showed that macromolecules possessing many proximal binding groups are more effective crystal growth modifiers than small molecules (e.g., the constituent monomers of polymeric modifiers).[69]

The use of CTAB as a modifier also yielded smaller crystals (192 ± 26 nm, Figure 6D); however, these samples appeared to

DOI: 10.1021/jacs.5b07477
J. Am. Chem. Soc. 2015, 137, 13007−13017

be more aggregated than those formed in the presence of PEIM. One disadvantage of CTAB is its stronger binding affinity to SSZ-13 crystals. Notably, as synthesized materials extracted from growth solutions contained an appreciable amount of residual CTAB that could not be removed by water washings. Powder XRD patterns revealed the presence of broad peaks that differed from the control sample (Figure S14). Calcination of these samples at 550 °C to remove CTAB yielded pristine crystalline peaks, but also revealed the presence of a minor impurity phase. Collectively, the results of $D6_{1,2}$ and CTAB experiments indicate that PEIM is the most efficient inhibitor of SSZ-13 crystallization among the modifiers that were tested.

Effects of a Positively Charged Polymer. Our prior work showed that neutral and charged ZGMs can have dramatically different effects on the preferential growth of zeolite crystals.[69] Motivated by this work, we assessed SSZ-13 growth in the presence of poly(diallyldimethylammonium chloride), or PDDAC, which is a polymer containing positively charged quaternary amines (see Table 1). Introduction of PDDAC in SSZ-13 growth solutions has the opposite effect of PEIM. Specifically, PDDAC promotes the formation of crystals with an average size of 23 ± 8 μm (Figure 7A), which is an order of magnitude larger than that of control crystals. PDDAC-modified crystals are faceted cubes (Figure 7B) with the family of {100}, {010}, and {001} crystallographic faces defining the sides of the cube. In SEM images, these surfaces appear to be macroscopically smooth; however, high resolution AFM images reveal the presence of hillocks (Figure 7C) with an average step height of 1.2 nm that is approximately equal to the unit cell dimension of the CHA framework ($a = b = 1.4$ and $c = 1.5$ nm). Terraced surfaces are characteristic features of crystals that grow via a 2D layer-by-layer mechanism. The presence of hillocks suggests that a classical pathway involving the addition of molecules plays a role in SSZ-13 crystallization. Interestingly, the center of each hillock contains a small deposit with nearly uniform size (ca. 7 nm in height). These deposits are observed on every hillock in AFM images (additional examples are provided in Figure S16). They appear to be the center of screw dislocations, and possibly the origin of layer nucleation and spreading. Indeed, the ubiquitous presence of these deposits in multiple samples and their uniform size suggests that they are not merely artifacts. The putative role of these deposits in layer growth, however, is unknown and cannot be easily discerned from ex situ AFM topographical images.

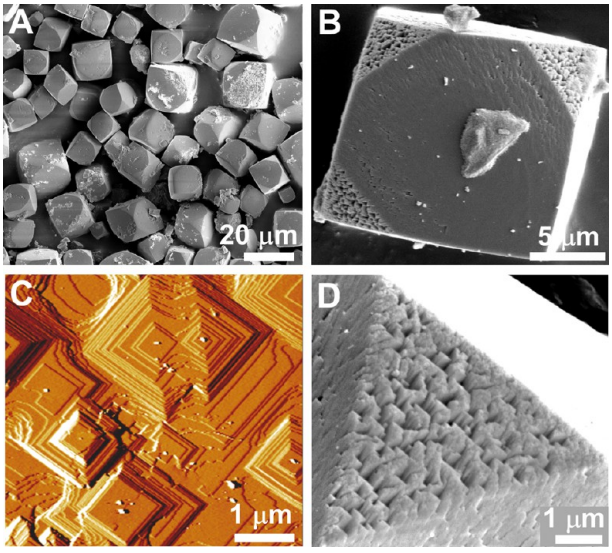

Figure 7. (A, B) Electron micrographs of SSZ-13 crystals prepared with PDDAC. (C) AFM amplitude mode image of the crystal surface (side of the cube) reveals the presence of hillocks comprised of single layers with ca. 1.2 nm step height. (D) High resolution SEM image of the crystal (corner of the cube) reveals a rough, porous surface.

AFM measurements of SSZ-13 crystals prepared with PDDAC occasionally reveal the presence of cracks on their surfaces that expose macropores (Figure S16A). SEM images also reveal the presence of distinct facets on the corners of the cubes that are macroscopically rough (Figure 7D). These observations prompted a textural analysis of SSZ-13 crystals. Argon adsorption/desorption and BET analysis showed that crystals prepared with PDDAC exhibit much higher specific surface area relative to the control (Table 2). Notably, control crystals have a surface area of 508 m^2/g and a type 1 adsorption isotherm (Figure 8, i), characteristic of microporous materials.

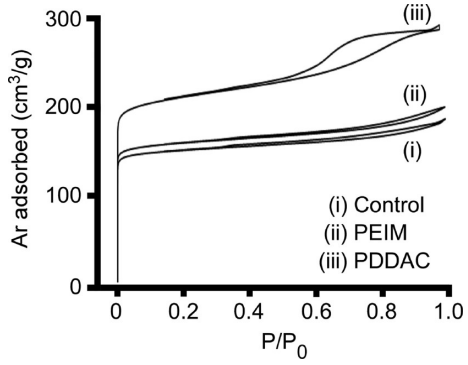

Figure 8. Ar adsorption and desorption isotherms of SSZ-13 crystals. The control sample (i) and PEIM sample (ii) exhibit type I isotherms, which are characteristic of microporous materials. The PDDAC sample (iii) exhibits a type IV isotherm, indicating the presence of mesopores. A *t*-plot analysis for micropore and external surface area are provided in Table S1 of the SI.

Similar results were obtained for crystals prepared with PEIM (Figure 8, ii); however, the crystals prepared with PDDAC have a surface area of 695 m^2/g and a type IV adsorption isotherm (Figure 8, iii), revealing the presence of mesopores, which is qualitatively consistent with SEM and AFM images. This is not entirely unexpected given that PDDAC seemingly promotes the rapid addition of precursors to crystal surfaces, increasing the probability of generating defects (e.g., mesoporous voids). If we consider pore sizes between 1.7 and 300 nm, the BJH adsorption cumulative surface area contribution to the total surface area is 92 m^2/g (i.e., 13% of the measured surface area of PDDAC-modified crystals). In order to determine if polymer is occluded within mesopores or on exterior surfaces of SSZ-13 crystals, we performed TGA measurements and found that the mass loss of organics (13.5 wt %, Table 2) and the temperature-programmed TGA profile (Figure S15) for PDDAC samples are identical to those of the control. This indicates that PDDAC is not occluded within crystals (note that the inclusion of all PDDAC added to the growth solution would result in an approximate 2.5% weight loss, assuming 100% yield of crystalline product). Additional properties of PDDAC-modified crystals were tested to check for potential side effects of the polymer. As listed in Table 2, there is little change in the Si/Al

DOI: 10.1021/jacs.5b07477
J. Am. Chem. Soc. 2015, 137, 13007−13017

ratio and a marginal increase in the percentage of extra-framework aluminum. Powder XRD also confirmed that the product is fully crystalline and devoid of any impurity (Figure S17).

Time-resolved ex situ studies of SSZ-13 crystallization in the presence of PDDAC were carried out over a 54 h period. Powder XRD revealed that samples extracted between 24 and 28 h of heating were predominantly amorphous (Figure S18). XRD analysis of the 28 h sample revealed the onset of Bragg peaks, while SEM images of this sample (Figure 9A) confirmed

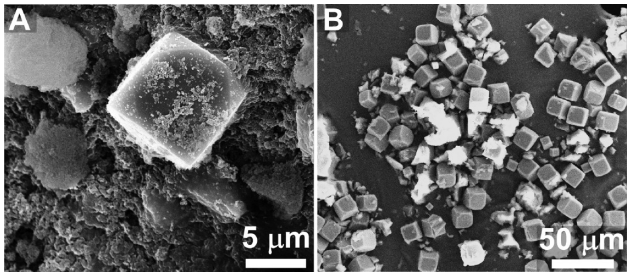

Figure 9. Scanning electron micrographs of samples extracted from a SSZ-13 growth solution containing 0.5 wt % PDDAC after (A) 28 h and (B) 29 h of heating at 180 °C. (C) Powder XRD patterns (Figure S18) of samples extracted from growth solutions at different heating times show a relatively rapid amorphous-to-crystalline transition.

the presence of multiple species: cubic crystals (<10 μm), spheroidal aggregates, and a larger population of amorphous WLPs. Surprisingly, one additional hour of heating was sufficient to produce an almost purely crystalline sample composed of ca. 20 μm cubic crystals (Figure 9B, 29 h) and very few WLPs. After 30 h heating, the product is fully crystalline (Figure S18). This is a significantly shorter synthesis time compared to the control, which requires approximately 50 h for completion. Moreover, PDDAC reduces the induction period by nearly 10 h. The exact time corresponding to the apparent "burst" in nucleation can vary from batch to batch by several hours; and the rapid time frame of crystal growth, which was consistently observed in more than 3 batches, makes it challenging to capture intermediate stages of crystallization from ex situ SEM or TEM images. Along these lines, there are many unanswered questions pertaining to the fundamental mechanism(s) by which PDDAC reduces nucleation time, increases the rate of crystal growth, and promotes the formation of large, faceted, and mesoporous SSZ-13 crystals.

Synergistic Effects of SSZ-13 Modifiers. Here we investigated the impact of using a combination of two modifiers that impose disparate effects on SSZ-13 crystallization. Binary mixtures were comprised of PDDAC, which produces large (ca. 20 μm) cubic crystals, and a second modifier (either PEIM or $D6_{1,2}$) that produce small (ca. 0.2 μm) spheroidal crystals. As shown in Figure 10A, the combination of 0.5 wt % PDDAC and 1.6 wt % PEIM results in the formation of crystals with an intermediate size (7.7 μm) and cubic morphology. The synergistic action of these polymers is evident by the formation of faceted crystals due to the presence of PDDAC and much smaller size than PDDAC-modified crystals, presumably due to the presence of PEIM. When the quantity of PDDAC is lowered by one-half, the average size of cubic crystals can be reduced to 4.2 μm (Figure S19). Further reduction in the size of cubic crystals could potentially be achieved by finding an optimal combination of either higher PEIM concentration or

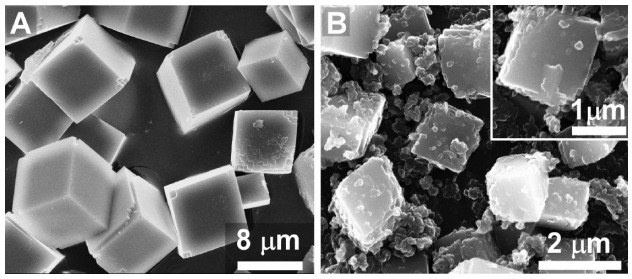

Figure 10. SEM images depicting the synergy between two additives that exhibit opposite effects, but when combined have a cooperative impact on crystal size and habit. Syntheses were performed with the following binary mixtures: (A) PDDAC (0.5 wt %) + PEIM (1.6 wt %) and (B) PDDAC (0.5 wt %) + $D6_{1,2}$ (13.3 wt %). Powder XRD patterns of all binary combinations are provided in Figure S19 of the SI.

lower PDDAC concentration. To this end, our study highlights the ability to rationally design SSZ-13 via the judicious selection of growth modifier combinations, thereby offering precision in crystal size that is unmatched by conventional routes.

A second binary combination of PDDAC and $D6_{1,2}$ produced a similar effect as the previous example, with two notable exceptions: (i) SSZ-13 crystals are more polydisperse in both size and shape owing to the presence of $D6_{1,2}$; and (ii) the size of cubic SSZ-13 crystals is generally smaller than the previous binary combination. SEM images reveal that a fraction of crystals modified with PDDAC−$D6_{1,2}$ mixtures are cubic with an average dimension of 1.4 μm, but there is also a significant population of both small and large spheroidal crystals (Figure 10B). The ability to generate smaller crystals in the PDDAC−$D6_{1,2}$ binary mixture is attributed to the high weight percentage of $D6_{1,2}$ that can be used to prepare SSZ-13 growth solutions without inducing the formation of an amorphous product. The same degree of tunability cannot be achieved using PEIM, which has a propensity to suppress crystallization at higher concentrations.

■ CONCLUSION

In summary, we have shown that SSZ-13 crystallization involves a complex mechanism. Evidence compiled primarily from time-resolved ex situ microscopy reveals that growth occurs by the addition of precursors (nonclassical pathway) and molecules (classical pathway). SSZ-13 growth solutions are viscous slurries containing amorphous aluminosilicate solids that, over the course of heating, transition from spheroidal aggregates to branched wormlike particles. These precursors are present throughout crystallization; their number density progressively decreasing in favor of a growing population of crystals. Our studies reveal that the induction period for nucleation is approximately 30 h, which is markedly longer than the time frame of crystal growth (ca. 10 h). The first nuclei observed in electron micrographs have macroscopically rough surfaces with feature sizes and geometries that mimic those of precursors. The formation of SSZ-13 crystals with spheroidal (nonfaceted) habit and rough surface features is evidence for growth by particle attachment. HRTEM images show the presence of spheroidal protrusions on crystal surfaces with an average diameter equal to the width of WLPs. In close proximity to crystal surfaces, we also identified the presence of small particulates (<10 nm). Neither the amorphous bulk phase nor the supernatant solution contains these particles, suggesting

DOI: 10.1021/jacs.5b07477
J. Am. Chem. Soc. 2015, 137, 13007−13017

they are a byproduct of the amorphous-to-crystalline transition that accompanies precursor attachment to SSZ-13 crystals. As such, these smaller particles may be intermediate species that form via solution-mediated processes (e.g., ripening) associated with the structural transformation of precursors after/during their attachment to crystal surfaces. AFM topographical images are qualitatively consistent with this proposed mechanism of growth. Notably, AFM images of SSZ-13 crystal surfaces reveal the presence of 3D islands with step heights that are markedly larger than those expected for classical 2D layer growth. After a prolonged heating time, we detect the coarsening of surface features and, under certain growth conditions, we also observe hillocks comprised of unfinished single layers. These two observations are indicative of classical growth; therefore, it is likely that crystals grow by a concomitant addition of molecules and particles. The latter appears to be the dominant pathway, whereas the former is more pronounced at later stages of growth when the population of WLPs is substantially diminished.

We demonstrate that growth modifiers are an efficient and cost-effective method to selectively tailor SSZ-13 crystal size and habit. The polymer PEIM, and to a lesser extent the organic molecule $D6_{1,2}$ and surfactant CTAB, were found to be effective inhibitors of SSZ-13 growth. Indeed, a small modifier concentration (<2 wt %) in SSZ-13 growth solutions is sufficient to produce 100 nm spheroidal crystals. PEIM's putative mode of action likely involves the inhibition of precursor attachment to crystals, akin to the role of a colloidal stabilizer, which leads to crystals that are an order of magnitude smaller than the control. In contrast, SSZ-13 crystallization in the presence of PDDAC produces faceted cubic crystals with an average size of 20 μm (i.e., an order of magnitude larger than the control). We observed that the presence of PDDAC in growth solutions reduces the nucleation time, leads to more rapid crystallization, and generates mesopores in SSZ-13 crystals. Thermogravimetric analysis of the residual organic content in crystals confirmed that very little modifier is retained within the product, suggesting that washing with water is sufficient to remove the organic modifiers. The facile recovery of modifiers and the potential for recycling highlight an economic advantage of this approach.

The degree to which SSZ-13 crystal size and shape is tuned by modifiers cannot be matched by conventional synthesis methods. Using a variety of commercially available modifiers, we can selectively alter crystal size from 0.1 to 20 μm. Our findings open new possibilities for testing SSZ-13 in a wide variety of commercially relevant applications to establish quantitative structure-performance relationships. Likewise, the nonclassical mechanism and multifaceted dynamics of SSZ-13 crystallization may prove to be more broadly representative of other zeolites by virtue of the similarity in precursors and growth solution compositions among numerous framework types. Indeed, fundamental knowledge of growth pathways holds the promise for predictively controlling materials synthesis, and designing more efficient methods to tailor their physicochemical properties.

■ ASSOCIATED CONTENT

Supporting Information

The Supporting Information is available free of charge on the ACS Publications website at DOI: 10.1021/jacs.5b07477.

Details of materials characterization are provided, including XRD patterns, supplemental SEM and TEM images, TGA profiles, elemental analysis (ICP-OES and EDX), DLS and SAXS data, solid state NMR, AFM topographic images and height profiles, *t*-plot analysis of Ar adsorption/desorption data, and examples of alternative modifiers that were tested (PDF)

■ AUTHOR INFORMATION

Corresponding Author

*jrimer@central.uh.edu

Notes

The authors declare no competing financial interest.

■ ACKNOWLEDGMENTS

We are grateful to Joel Schmidt at the California Institute of Technology for performing solid-state NMR experiments. The work at UH was supported by funding from the National Science Foundation (Award No. 1151098) and The Welch Foundation (Award No. E-1794). The work at MIT was supported by funding from the Chemical Sciences, Geosciences and Biosciences Division, Office of Basic Energy Sciences, U.S. Department of Energy (Award No. DE-FG0212ER16352).

■ REFERENCES

(1) De Yoreo, J. J.; Gilbert, P. U. P. A.; Sommerdijk, N. A. J. M.; Penn, R. L.; Whitelam, S.; Joester, D.; Zhang, H.; Rimer, J. D.; Navrotsky, A.; Banfield, J. F.; Wallace, A. F.; Michel, F. M.; Meldrum, F. C.; Cölfen, H.; Dove, P. M. *Science* **2015**, *349*, 6247.

(2) Liao, H. G.; Cui, L. K.; Whitelam, S.; Zheng, H. M. *Science* **2012**, *336*, 1011.

(3) Zheng, H. M.; Smith, R. K.; Jun, Y. W.; Kisielowski, C.; Dahmen, U.; Alivisatos, A. P. *Science* **2009**, *324*, 1309.

(4) Li, D. S.; Soberanis, F.; Fu, J.; Hou, W. T.; Wu, J. Z.; Kisailus, D. *Cryst. Growth Des.* **2013**, *13*, 422.

(5) Raju, M.; van Duin, A. C. T.; Fichthorn, K. A. *Nano Lett.* **2014**, *14*, 1836.

(6) Hould, N. D.; Foster, A.; Lobo, R. F. *Microporous Mesoporous Mater.* **2011**, *142*, 104.

(7) Banfield, J. F.; Welch, S. A.; Zhang, H. Z.; Ebert, T. T.; Penn, R. L. *Science* **2000**, *289*, 751.

(8) Ge, J. P.; Hu, Y. X.; Biasini, M.; Beyermann, W. P.; Yin, Y. D. *Angew. Chem., Int. Ed.* **2007**, *46*, 4342.

(9) Baumgartner, J.; Dey, A.; Bomans, P. H. H.; Le Coadou, C.; Fratzl, P.; Sommerdijk, N.; Faivre, D. *Nat. Mater.* **2013**, *12*, 310.

(10) Van Driessche, A. E. S.; Benning, L. G.; Rodriguez-Blanco, J. D.; Ossorio, M.; Bots, P.; Garcia-Ruiz, J. M. *Science* **2012**, *336*, 69.

(11) Yau, S. T.; Vekilov, P. G. *J. Am. Chem. Soc.* **2001**, *123*, 1080.

(12) Addadi, L.; Weiner, S. *Angew. Chem., Int. Ed. Engl.* **1992**, *31*, 153.

(13) He, G.; Dahl, T.; Veis, A.; George, A. *Nat. Mater.* **2003**, *2*, 552.

(14) Nielsen, M. H.; Aloni, S.; De Yoreo, J. J. *Science* **2014**, *345*, 1158.

(15) Gal, A.; Weiner, S.; Addadi, L. *CrystEngComm* **2015**, *17*, 2606.

(16) Lupulescu, A. I.; Rimer, J. D. *Science* **2014**, *344*, 729.

(17) Davis, T. M.; Drews, T. O.; Ramanan, H.; He, C.; Dong, J.; Schnablegger, H.; Katsoulakis, M. A.; Kokkoli, E.; McCormick, A. V.; Penn, R. L.; Tsapatsis, M. *Nat. Mater.* **2006**, *5*, 400.

(18) Li, D. S.; Nielsen, M. H.; Lee, J. R. I.; Frandsen, C.; Banfield, J. F.; De Yoreo, J. J. *Science* **2012**, *336*, 1014.

(19) Yucelen, G. I.; Choudhury, R. P.; Vyalikh, A.; Scheler, U.; Beckham, H. W.; Nair, S. *J. Am. Chem. Soc.* **2011**, *133*, 5397.

(20) Cundy, C. S.; Cox, P. A. *Microporous Mesoporous Mater.* **2005**, *82*, 1.

(21) Ren, N.; Bosnar, S.; Bronic, J.; Sikiric, M. D.; Misic, T.; Svetlicic, V.; Mao, J. J.; Jelic, T. A.; Hadzija, M.; Subotic, B. *Langmuir* **2014**, *30*, 8570.

DOI: 10.1021/jacs.5b07477
J. Am. Chem. Soc. 2015, 137, 13007−13017

(22) Ren, N.; Subotic, B.; Bronic, J.; Tang, Y.; Sikiric, M. D.; Misic, T.; Svetlicic, V.; Bosnar, S.; Jelic, T. A. *Chem. Mater.* **2012**, *24*, 1726.
(23) Bosnar, S.; Antonic, T.; Bronic, J.; Subotic, B. *Microporous Mesoporous Mater.* **2004**, *76*, 157.
(24) Bosnar, S.; Subotic, B. *Croat. Chem. Acta* **2002**, *75*, 663.
(25) Deka, U.; Juhin, A.; Eilertsen, E. A.; Emerich, H.; Green, M. A.; Korhonen, S. T.; Weckhuysen, B. M.; Beale, A. M. *J. Phys. Chem. C* **2012**, *116*, 4809.
(26) Bates, S. A.; Verma, A. A.; Paolucci, C.; Parekh, A. A.; Anggara, T.; Yezerets, A.; Schneider, W. F.; Miller, J. T.; Delgass, W. N.; Ribeiro, F. H. *J. Catal.* **2014**, *312*, 87.
(27) Hudson, M. R.; Queen, W. L.; Mason, J. A.; Fickel, D. W.; Lobo, R. F.; Brown, C. M. *J. Am. Chem. Soc.* **2012**, *134*, 1970.
(28) Loiland, J. A.; Lobo, R. F. *J. Catal.* **2014**, *311*, 412.
(29) Bordiga, S.; Regli, L.; Lamberti, C.; Zecchina, A.; Bjorgen, M.; Lillerud, K. P. *J. Phys. Chem. B* **2005**, *109*, 7724.
(30) Regli, L.; Zecchina, A.; Vitillo, J. G.; Cocina, D.; Spoto, G.; Lamberti, C.; Lillerud, K. P.; Olsbye, U.; Bordiga, S. *Phys. Chem. Chem. Phys.* **2005**, *7*, 3197.
(31) Xie, L. J.; Liu, F. D.; Liu, K.; Shi, X. Y.; He, H. *Catal. Sci. Technol.* **2014**, *4*, 1104.
(32) Van Speybroeck, V.; Hemelsoet, K.; De Wispelaere, K.; Qian, Q. Y.; Van der Mynsbrugge, J.; De Sterck, B.; Weckhuysen, B. M.; Waroquier, M. *ChemCatChem* **2013**, *5*, 173.
(33) Goltl, F.; Bulo, R. E.; Hafner, J.; Sautet, P. *J. Phys. Chem. Lett.* **2013**, *4*, 2244.
(34) Kwak, J. H.; Tonkyn, R. G.; Kim, D. H.; Szanyi, J.; Peden, C. H. F. *J. Catal.* **2010**, *275*, 187.
(35) Martinez-Franco, R.; Moliner, M.; Thogersen, J. R.; Corma, A. *ChemCatChem* **2013**, *5*, 3316.
(36) Ren, L.; Zhu, L.; Yang, C.; Chen, Y.; Sun, Q.; Zhang, H.; Li, C.; Nawaz, F.; Meng, X.; Xiao, F. S. *Chem. Commun.* **2011**, *47*, 9789.
(37) Olsbye, U.; Svelle, S.; Bjorgen, M.; Beato, P.; Janssens, T. V. W.; Joensen, F.; Bordiga, S.; Lillerud, K. P. *Angew. Chem., Int. Ed.* **2012**, *51*, 5810.
(38) Jeon, H. Y.; Shin, C. H.; Jung, H. J.; Hong, S. B. *Appl. Catal., A* **2006**, *305*, 70.
(39) Bleken, F.; Bjorgen, M.; Palumbo, L.; Bordiga, S.; Svelle, S.; Lillerud, K. P.; Olsbye, U. *Top. Catal.* **2009**, *52*, 218.
(40) Deimund, M. A.; Schmidt, J. E.; Davis, M. E. *Top. Catal.* **2015**, *58*, 416.
(41) Fickel, D. W.; D'Addio, E.; Lauterbach, J. A.; Lobo, R. F. *Appl. Catal., B* **2011**, *102*, 441.
(42) Gao, F.; Walter, E. D.; Karp, E. M.; Luo, J. Y.; Tonkyn, R. G.; Kwak, J. H.; Szanyi, J.; Peden, C. H. F. *J. Catal.* **2013**, *300*, 20.
(43) Blakeman, P. G.; Burkholder, E. M.; Chen, H. Y.; Collier, J. E.; Fedeyko, J. M.; Jobson, H.; Rajaram, R. R. *Catal. Today* **2014**, *231*, 56.
(44) Colombo, M.; Nova, I.; Tronconi, E. *Catal. Today* **2010**, *151*, 223.
(45) Fedeyko, J. M.; Chen, B.; Chen, H. Y. *Catal. Today* **2010**, *151*, 231.
(46) Kwak, J. H.; Tran, D.; Szanyi, J.; Peden, C. H. F.; Lee, J. H. *Catal. Lett.* **2012**, *142*, 295.
(47) Kwak, J. H.; Tran, D.; Burton, S. D.; Szanyi, J.; Lee, J. H.; Peden, C. H. F. *J. Catal.* **2012**, *287*, 203.
(48) Giordanino, F.; Vennestrom, P. N. R.; Lundegaard, L. F.; Stappen, F. N.; Mossin, S.; Beato, P.; Bordiga, S.; Lamberti, C. *Dalton Trans.* **2013**, *42*, 12741.
(49) Zones, S. I. (Chevron Research Co.) U.S. Patent US4544538A, 1985.
(50) Zones, S. I.; Yuen, L.-T.; Miller, S. J. (Chevron U.S.A. Inc.) U.S. Patent US6709644B2, 2004.
(51) Itakura, M.; Inoue, T.; Takahashi, A.; Fujitani, T.; Oumi, Y.; Sano, T. *Chem. Lett.* **2008**, *37*, 908.
(52) Bohstrom, Z.; Arstad, B.; Lillerud, K. P. *Microporous Mesoporous Mater.* **2014**, *195*, 294.
(53) Dahl, I. M.; Wendelbo, R.; Andersen, A.; Akporiaye, D.; Mostad, H.; Fuglerud, T. *Microporous Mesoporous Mater.* **1999**, *29*, 159.
(54) Wu, L. L.; Degirmenci, V.; Magusin, P.; Lousberg, N.; Hensen, E. J. M. *J. Catal.* **2013**, *298*, 27.
(55) Wu, L. L.; Degirmenci, V.; Magusin, P.; Szyja, B. M.; Hensen, E. J. M. *Chem. Commun.* **2012**, *48*, 9492.
(56) Khare, R.; Millar, D.; Bhan, A. *J. Catal.* **2015**, *321*, 23.
(57) Nishiyama, N.; Kawaguchi, M.; Hirota, Y.; Van Vu, D.; Egashira, Y.; Ueyama, K. *Appl. Catal., A* **2009**, *362*, 193.
(58) Burton, W. K.; Cabrera, N.; Frank, F. C. *Philos. Trans. R. Soc., A* **1951**, *243*, 299.
(59) Kaishev, R.; Stranski, I. N. *Z. Phys. Chem.* **1934**, *B26*, 114.
(60) Greer, H. F. *Mater. Sci. Technol.* **2014**, *30*, 611.
(61) Niederberger, M.; Colfen, H. *Phys. Chem. Chem. Phys.* **2006**, *8*, 3271.
(62) Ju, R. T. C.; Frank, C. W.; Gast, A. P. *Langmuir* **1992**, *8*, 2165.
(63) Weissbuch, I.; Addadi, L.; Lahav, M.; Leiserowitz, L. *Science* **1991**, *253*, 637.
(64) Weiner, S.; Addadi, L. *J. Mater. Chem.* **1997**, *7*, 689.
(65) Stupp, S. I.; Braun, P. V. *Science* **1997**, *277*, 1242.
(66) Estroff, L. A.; Hamilton, A. D. *Chem. Mater.* **2001**, *13*, 3227.
(67) Sikiric, M. D.; Furedi-Milhofer, H. *Adv. Colloid Interface Sci.* **2006**, *128*, 135.
(68) Lupulescu, A. I.; Rimer, J. D. *Angew. Chem., Int. Ed.* **2012**, *51*, 3345.
(69) Lupulescu, A. I.; Kumar, M.; Rimer, J. D. *J. Am. Chem. Soc.* **2013**, *135*, 6608.
(70) Wiley, B.; Sun, Y. G.; Mayers, B.; Xia, Y. N. *Chem. - Eur. J.* **2005**, *11*, 454.
(71) Jo, C.; Jung, J.; Shin, H. S.; Kim, J.; Ryoo, R. *Angew. Chem., Int. Ed.* **2013**, *52*, 10014.
(72) Semagina, N.; Kiwi-Minsker, L. *Catal. Rev.: Sci. Eng.* **2009**, *51*, 147.
(73) Yu, S. H.; Colfen, H. *J. Mater. Chem.* **2004**, *14*, 2124.
(74) Teranishi, T.; Miyake, M. *Chem. Mater.* **1998**, *10*, 594.
(75) Orilall, M. C.; Wiesner, U. *Chem. Soc. Rev.* **2011**, *40*, 520.
(76) Huang, W.-C.; Lyu, L.-M.; Yang, Y.-C.; Huang, M. H. *J. Am. Chem. Soc.* **2012**, *134*, 1261.
(77) Yucelen, G. I.; Kang, D. Y.; Guerrero-Ferreira, R. C.; Wright, E. R.; Beckham, H. W.; Nair, S. *Nano Lett.* **2012**, *12*, 827.
(78) Si, R.; Zhang, Y. W.; You, L. P.; Yan, C. H. *J. Phys. Chem. B* **2006**, *110*, 5994.
(79) Nagaya, J.; Homma, M.; Tanioka, A.; Minakata, A. *Biophys. Chem.* **1996**, *60*, 45.

DOI: 10.1021/jacs.5b07477
J. Am. Chem. Soc. 2015, 137, 13007−13017